Check for updates

RESEARCH ARTICLE

WILEY SURFACE and INTERFACE ANALYSIS

Effect of deposition temperature on the growth mechanism of chemically prepared CZTGeS thin films

A. Shamardin[1] ⓘ | D. Kurbatov[1] ⓘ | A. Medvids[2]

[1] Department of Electronics and Computer Technology, Sumy State University, 2 Rymskogo Korsakova Str., Sumy 40007, Ukraine

[2] Institute of Technical Physics, Riga Technical University, 3/7, Paula Valdena Str., Riga LV-1048, Latvia

Correspondence
Shamardin Artem, Department of Electronics and Computer Technology, Sums'kij Derzhavnij Universitet, 2 Rymskogo Korsakova St, Sumy 40007, Ukraine.
Email: artemv.shamardin@gmail.com

The $Cu_2ZnSnGeS_4$ (CZTGeS) thin films were deposited by the spray pyrolysis method at different substrate temperatures without further sulfurization. The influence of various deposition temperatures on the surface morphology, microstructure, optical properties, chemical, and phase composition were investigated. The substitution mechanism of Sn/Ge in the crystal lattice of CZTGeS depending on deposition temperatures was studied. It was shown that a variation in substrate temperature has a strong effect on the surface morphology of the films. The X-ray diffractometer (XRD), transmission electron microscope (TEM), and Raman spectroscopy (RS) analysis showed that CZTGeS films were polycrystalline with a kesterite-type single-phase structure and a preferential orientation of (112). The RS-mapping analysis showed the distribution of intensities on the surfaces of the films. Optical measurements showed that CZTGeS films are highly absorbing in the visible region, and the optical band gap is shifted from 1.89 to 1.84 eV.

KEYWORDS

CZTGeS, optical properties, Raman mapping, spray pyrolysis, surface morphology, X-ray diffraction

1 | INTRODUCTION

Recent research in the field of development of thin film solar cells based on chalcopyrite $CuIn_xGa_{1-x}(S, Se)_2$ (CIGS/Se) has resulted into an increase of the cell efficiency up to 23.3% in the lab area.[1] However, the massive commercial production of CIGS solar cells, as expected, can be limited in the future because of the scarcity of In in the Earth's crust and its high cost value. In this regard, the most promising alternative material for CIGS absorber could be the chalcogenide compound of Cu_2ZnSnS_4 (CZTS) with a kesterite-type phase, which contains Zn and Sn instead of In and Ga.

CZTS has a high absorption coefficient ($\alpha > 10^4$ cm^{-1}), direct band gap ($E_g \sim 1.5$ eV), and p-type conductivity,[2,3] which allows for effective absorption of the most incident photons in absorbers with thicknesses of 1 to 2 µm. However, the current efficiency of CZTS-based solar cells does not exceed 12.6%,[4] because of the short lifetimes of minority charge carriers in the sub-nanosecond regime.[5] Despite the fact that the maximum possible efficiency of 32% (Shockley-Queisser limit) for CZTS-based solar cells has not been reached yet, the significant

advances in understanding the functioning problems of photovoltaic devices were achieved.

The main problem of performance limitation in CZTS-based solar cells is the low open-circuit voltage (V_{oc}). In addition, it is difficult to obtain a high purity compound, because the bounded stability region in the phase diagram of CZTS provides conditions for the easy formation of secondary phases such as Cu_2SnS_3, Cu_xS_y, and Zn_xS_y.[6-8] In a recent study,[9] a new approach, allowing to increase the solar conversion efficiency of kesterite-based devices, was proposed. The authors of this work offered a partially controlled substitution of Sn cations by Ge ones. In accordance with the proposed hypothesis, the Ge–S bonds are stronger than Sn–S bonds. Substitution of Sn atoms by the smaller Ge atoms leads to an enhanced repulsion between the s–s and s–p levels of Ge and S, which increases the antibonding character of conduction band minimum.[10] These assumptions were confirmed in theoretical[11] and experimental works.[12]

There are numerous methods for deposition of $Cu_2ZnSnGeS_4$ (CZTGeS) thin films, which including the magnetron sputtering,[13] colloidal synthesis,[14] knife coating,[15] solvothermal synthesis,[16] spray

pyrolysis,[17] etc. The last method attracts a considerable attention because it is easy to implement, it has a high controllability of parameters and requires a cheap manufacturing equipment.[18,19] Nevertheless, the substitution mechanism of Sn by Ge in CZTGeS thin films, obtained at different deposition temperatures by the method of spray pyrolysis, is not sufficiently studied yet.

In this work, we have prepared CZTGeS thin films by spray pyrolysis method. Their structural, morphological, and optical properties were investigated. The influence of various deposition temperatures on the substitution mechanism of Sn/Ge in thin films was studied.

2 | EXPERIMENTAL PART

$CuCl_2$ (99%), $ZnCl_2$ (99%), $SnCl_2 + 2H_2O$ (99%), GeO_2 (99.999%, β-quartz type of crystal structure), CH_4N_2S (99%), and dimethyl sulfoxide (DMSO) were purchased from Acros Organics, Merck, and Sigma Aldrich. All reagents and solvent were used in their original form without preliminary purification. The initial precursor of CZTGeS included $CuCl_2$ (25 mmol), $ZnCl_2$ (12.5 mmol), $SnCl_2 + 2H_2O$ (7.5 mmol), GeO_2 (5 mmol), and CH_4N_2S (50 mmol) with a molar ratio of 2:1:0.6:0.4:8, respectively. Synthesis of the initial precursor was carried out in two stages. In the first stage, $CuCl_2$, $ZnCl_2$, $SnCl_2 + 2H_2O$, and CH_4N_2S were dissolved in DMSO. The GeO_2 powder was dissolved in distilled water at the temperature of 80°C to 90°C and cooled to a room temperature naturally. In the second stage, both solutions were mixed in a chemical glassware.

The experimental spray system was used for deposition of CZTGeS thin films. The final precursor was sprayed on soda-lime glass substrates at different temperatures (T_S from 598 to 698 K, in increments of 25 K). Argon was used as a carrier gas. In order to obtain the homogeneous films with a good adhesion to substrate, the pulsed mode of sputtering was used. The spraying time was 2 seconds with a 5 seconds pause between cycles. The number of cycles was 250 units.

To study the chemical composition, a scanning electron microscope Selmi PEMMA 106-I with an integrated energy dispersive spectroscopy (EDS) was used. For precise investigation of surface morphology, the atomic force microscope (AFM) NT-MDT in the contact error mode was used. The phase composition of the films and their microstructure were investigated using a transmission electron microscope (TEM) Selmi PEM-125K in light and microdiffraction modes with the accelerating voltage of 90 keV. The structural analysis was performed using the X-ray diffractometer (XRD) DRON-3 in the Bragg-Brentano geometry in Kα radiation of the copper anode (λ = 1.54018 Å). The scanning step was 0.05° and the range of the diffraction angles 2θ was from 20° to 80°. The average size of coherent scattering region (CSR, L) and microstrain (ε) were determined by Williamson-Hall plot from the following equation:

$$\beta_{hkl}\cos\theta = \frac{k\lambda}{L} + 4\varepsilon\sin\theta, \tag{1}$$

where β is the physical extension of the corresponding X-ray line. The parameters a and c of the tetragonal crystal lattice were determined by the following equations:

$$a = \frac{\lambda}{2\sin\theta}\sqrt{h^2 + k^2 + l^2\left(\frac{a}{c}\right)^2}, \tag{2}$$

$$c = \frac{l}{\sqrt{-\frac{h^2+k^2}{a^2} + \left(\frac{2\sin\theta}{\lambda}\right)^2}}, \tag{3}$$

where λ is the wavelength of X-rays, θ is the Wolf-Bragg angle, and h, k, l are the Miller indices. To clarify the values of lattice parameters (a, c), the extrapolative method of Nelson-Riley, which included 10 mathematical iterations, was used.[20] The linear approximation of the obtained values was performed using the least-squares method. In order to increase the precision of the lattice parameters values, the graphic method of consecutive approximations was used. The pole density value was calculated from the following equation[21,22]:

$$P_i = \frac{(I_i/I_{0i})}{\frac{1}{N}\sum_{i=1}^{N}(I_i/I_{0i})}, \tag{4}$$

where I_i and I_{0i} are the intensities of the ith diffraction peak of deposited film and etalon from the reference data, respectively, and N is the number of lines on the radiograph. The orientation factor of the films was determined by the following equation[23,24]:

$$f = \sqrt{\frac{1}{N}\sum_{i=1}^{N}(P_i-1)^2}, \tag{5}$$

The Raman spectroscopy mapping analysis (RS-mapping) was performed at a room temperature with the Renishaw InVia90V727 Raman microscope in backscattering geometry with excitation by a near-infrared laser (λ = 785 nm). The RS measurements were performed on a motorized table with the scanning area of 100×100 μm². The excitation power and exposure time values of the laser were set in such a way to obtain a high signal-to-noise ratio of the spectra without damaging the surface of the sample because of its local heating.

The optical properties were studied using the Lasany Visible LI-722 spectrophotometer in the wavelength range of λ = 340 to 1000 nm at a room temperature. Optical band gap (E_g) of the material was calculated from the transmission spectra using the following equation:

$$\alpha h\vartheta = A(h\vartheta - E_g)^2, \tag{6}$$

where α is the absorption coefficient, $h\upsilon$ is the photon energy, and A is a constant, which depends on the effective mass of charge carriers in the material. The absorption coefficient was calculated from the following equation:

$$a = \frac{\ln\left(\frac{100}{T}\right)}{d}, \tag{7}$$

where T is the transmittance spectra (in %) and d is the thickness of the film. Calibration of the transmittance spectra was performed by preliminary measurement of the transmittance spectra from the substrate material. In order to control the overall thickness of the films, the interferometer MII-4 (Linnyka) was used.

3 | RESULTS AND DISCUSSION

3.1 | Surface morphology and chemical composition

In Figure 1, the profile of deflection (DFL) images (1), surface topography 3D-images (2), and microstructures (3) of CZTGeS thin films deposited at different temperatures are presented. The scanning area for all AFM micrographs was 250 μm^2. It is well demonstrated (Figure 1A(2)) that the surface of the film deposited at T_S = 598 K consisted of small craters with an average diameter of 15 μm. These craters are formed from droplets during spraying a precursor. When the deposition temperature increased to T_S = 623 K, the film surface became quite smooth and uniform throughout the plane. Herewith, for this film (Figure 1B(2)), the root mean square roughness (RMS) and average surface roughness (ASR) show the minimum values of

78.9 nm and 62.6 nm, respectively. Increasing of deposition temperature (Figure 1C(2)) has led to the formation of a significant number of micron-size heterogeneities on the surface. The reason for this could be the coalescence and reorganization of the material. At higher deposition temperatures (T_S = 673-698 K), we observed an agglomeration of these heterogeneities with the formation of deep craters. It should be noted that the RMS and ASR values of the films are increased with increasing of deposition temperature, except the sample obtained at T_S = 623 K. At the same time, thin films did not contain cracks or voids in this study.

It is clearly seen from the TEM images (Figure 1A-E(3)) that a crystallization process takes place in the temperature region of T_S = 623-648 K, which was also observed in similar works, but only for CZTS thin films.[25-27] For these samples, the average diameter of crystallites lies in the region of 16 to 17 nm. In the case of the deposition with the lowest temperature (Figure 1A), the film is heterogeneous and only partially include crystallites. Higher deposition temperatures led to a reduction of the crystallite sizes (Figure 1D,E). The nonmonotonic change in the sizes of nanocrystals depending on the deposition temperature can be explained by the following assumption: At lower temperatures, there is a sufficient amount of thermal energy for the growth of large crystals, but at higher temperatures
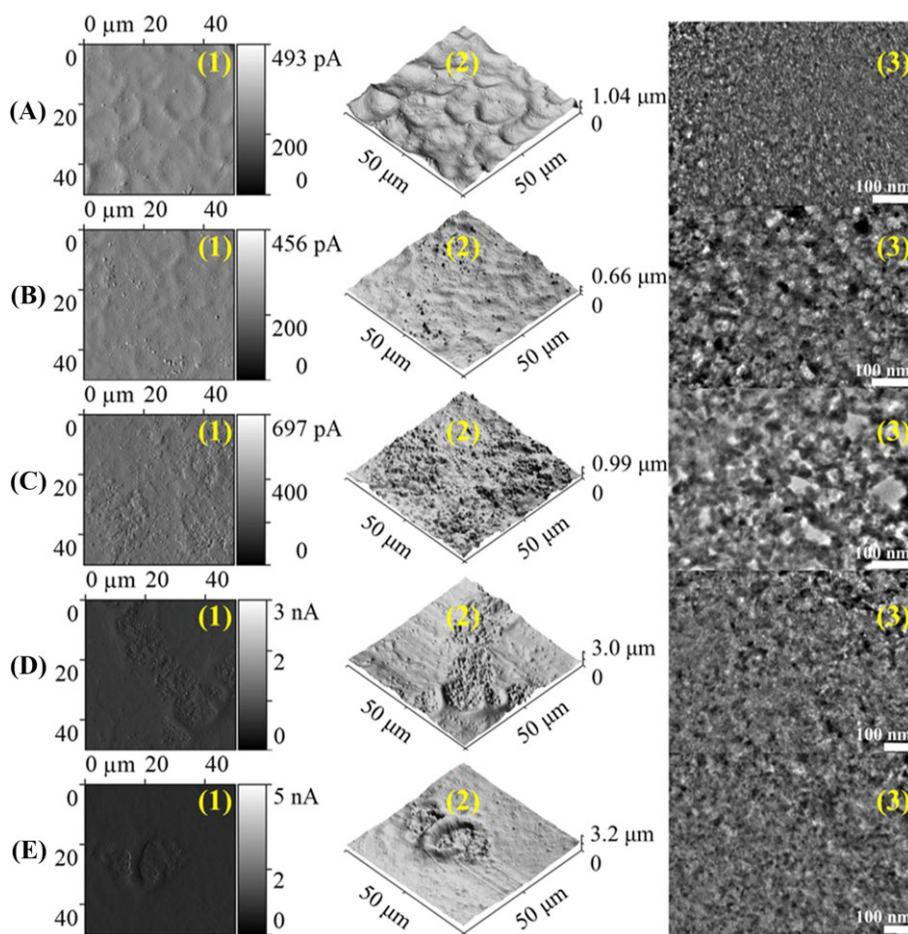
FIGURE 1   The DFL images (1), surface topography of 3D images (2) and microstructures (3) of CZTGeS thin films deposited at T_S, K: 598 (A), 623 (B), 648 (C), 673 (D), 698 (E)

(more than 648 K), crystallites decrease in sizes under the influence of rapid displacements of atoms.

In Table 1, the chemical composition of CZTGeS thin films is presented. Results of the analysis clearly show that each film is Cu and Zn rich, but S poor. The low concentration of S in the samples could be related to its low boiling point ($T_{Sulphur}$ = 717.75 K), which is very close to the deposition temperature, especially, for the last sample (T_S = 698 K). The higher deposition temperature can reduce the impact of S on the phase formation process in a thin film. It is confirmed by the decreasing of S concentration with increasing of T_S up to 698 K. As a result, the chemical concentration of the components in as-deposited films differs from the stoichiometric values of the initial precursor.

The concentration of Sn increased with increasing of the deposition temperature, except the sample obtained at T_S = 673 K, which could be caused by the error of the measurement method.[28] The concentration of Ge has the maximal value at T_S = 623 K, but it is gradually decreased in the region of T_S = 648 to 698 K. The ratios of Ge/Sn + Ge and S/Cu + Zn + Sn + Ge are reduced with increasing of the deposition temperature.

It can be concluded from results of the chemical analysis (Table 1) that the deposited thin films have a nonstoichiometric composition, but concentrations of the components are within the acceptable range for the formation of CZTGeS compound.[29]

3.2 | Phase composition

The diffraction patterns of CZTGeS thin films, deposited at different temperatures, are shown in Figure 2. On each radiograph (Figure 2), peaks are observed, which correspond to the reflections of crystallographic planes (112), (220), and (312) from CZTS with a kesterite-type phase.[30-32] As the deposition temperature increased, the peaks position did not actually change; however, the intensity of the main peak (112) decreased and the intensity of the peaks (220) and (312) increased.

It is well known that the value of the lattice constant is a property that is extremely sensitive to changes in the stoichiometric composition,[33] as well as to the presence of impurities,[34] etc. Accurate calculation of these values makes it possible to study the corresponding

TABLE 1 Chemical compositions of CZTGeS thin films

Sample	T_S, K	Cu (at .%)	Zn (at .%)	Sn (at .%)	Ge (at .%)	S (at .%)	Cu/(Zn + VI)	S/M	Ge/VI
CZTGeS	598	28.22	13.33	8.42	4.21	45.83	1.09	0.85	0.33
	623	26.84	13.44	8.91	4.96	45.86	0.98	0.85	0.36
	648	26.08	13.96	9.79	4.58	45.59	0.92	0.84	0.32
	673	26.44	13.39	9.59	4.22	46.37	0.97	0.87	0.31
	698	26.59	13.55	10.97	4.31	44.59	0.92	0.81	0.28

Note. VI = Sn + Ge; M = Cu + Zn + VI.
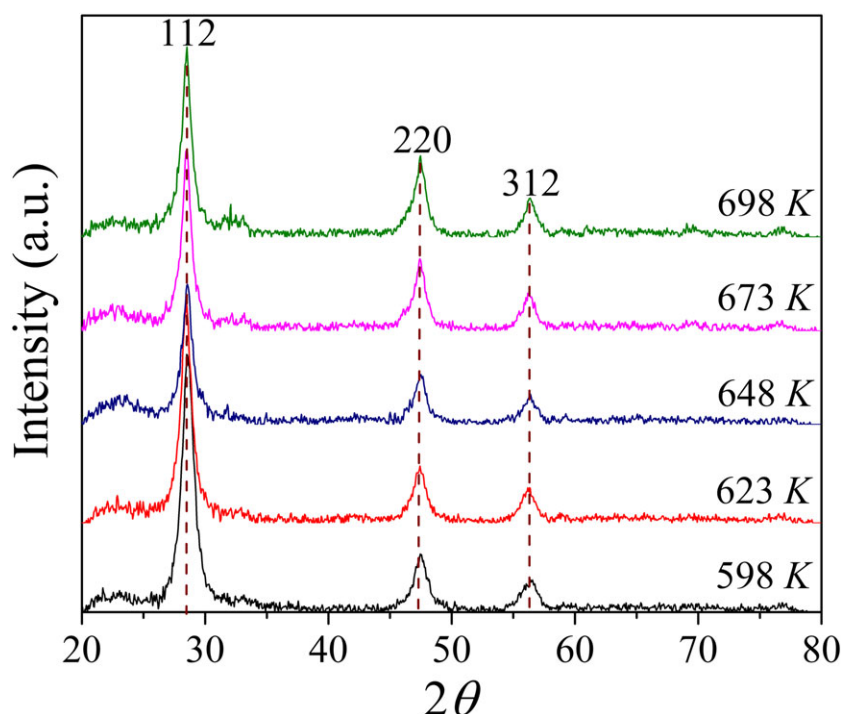
FIGURE 2 X-ray diffractometer (XRD) patterns from CZTGeS thin films

processes occurring in the crystal structure. By 10 mathematical iterations, described above, the lattice parameters (a, c) of CZTGeS films were calculated. The results are shown in Table 2.

The dependences of lattice parameters (a, c) on the deposition temperature, based on the data from Table 2, is shown in Figure 3. As it is shown in Figure 3, these parameters are gradually increased with increasing of T_S up to 648 K and, accordingly, the volume of the crystal lattice is increased too. It can be related with increasing the chemical concentration of Sn atoms, which have the largest atomic mass among all components in CZTGeS. This assumption is confirmed by the data from EDS analysis in Table 1. In the region of T_S = 673 to 698 K, the lattice parameter c is decreased, but the lattice parameter a is decreased only at T_S = 698 K. It indicates that defects appear in the crystal lattice of a film deposited at T_S = 673 K; namely, the lattice shrinkage effect takes place. This effect leads to the formation of tensile stress since the smaller Ge atoms rapidly replace the larger Sn atoms in the crystal lattice.[35] In the case of T_S = 698 K, the following situation is observed. It is well known that in the crystal lattice of CZTS, the Sn atom is always located at the 2b (1/2,1/2,0) Wyckoff position.[36] Therefore, microstrains in the crystal lattice decrease at T_S = 698 K, since Ge atoms begin to occupy positions of Sn atoms, which reduces the volume of the crystal lattice.

Calculations of the pole density P_i from data in Table 2 is shown in Figure 4. From these results, it was determined an axial texture growth in the (112) direction for each CZTGeS thin film. However, with increasing of the deposition temperature up to 648 K, it is observed that an axial texture growth is gradually decreased in the (112) direction and increased in the (220) and (312) directions. In the region of higher temperatures, T_S = 648 to 698 K, the texture growth takes a linear form. In the inset (Figure 5), the dependence of the orientation factor f on the deposition temperature is shown. As it is seen from the inset, increasing of the deposition temperature has reduced the orientation factor, pointing to a deterioration in the texture quality of thin films obtained at higher T_S.

The calculated CSR value shows a tendency of increasing at higher T_S. At T_S = 673 K, the CSR and ε have negative values, which is an additional confirmation of the lattice shrinkage effect in this thin film. As is known, increasing of CSR is associated with increasing of the crystalline domain size.[37] Thus, CZTGeS films, deposited at T_S = 648 K and T_S = 698 K, have a lower concentration of dislocations in comparison with other films in this study. However, the film deposited at T_S = 623 K has optimal parameters among all samples in this experiment, such as CSR, P_i, and f.

In order to confirm the results of the XRD analysis, the samples were measured by TEM. The corresponding selected area diffraction

**TABLE 2** Calculations of the lattice parameters of thin films

T_S, K	Lattice Parameters, nm		$L_{(W-H)}$, nm	$\varepsilon_{(W-H)} \times 10^{-3}$	Pole Density, P_i			Orientation factor, f
	a	c			(112)	(220)	(312)	
598	0.5406	1.0416	7.1	1.54	5.12	1.29	2.59	2.55
623	0.5409	1.0521	8.6	2.30	4.66	1.34	3.01	2.42
648	0.5411	1.0776	8.5	0.65	3.96	1.56	3.48	2.25
673	0.5416	1.0715	-	-	3.97	1.76	3.27	2.20
698	0.5405	1.0539	9.0	0.69	3.91	1.86	3.23	2.17
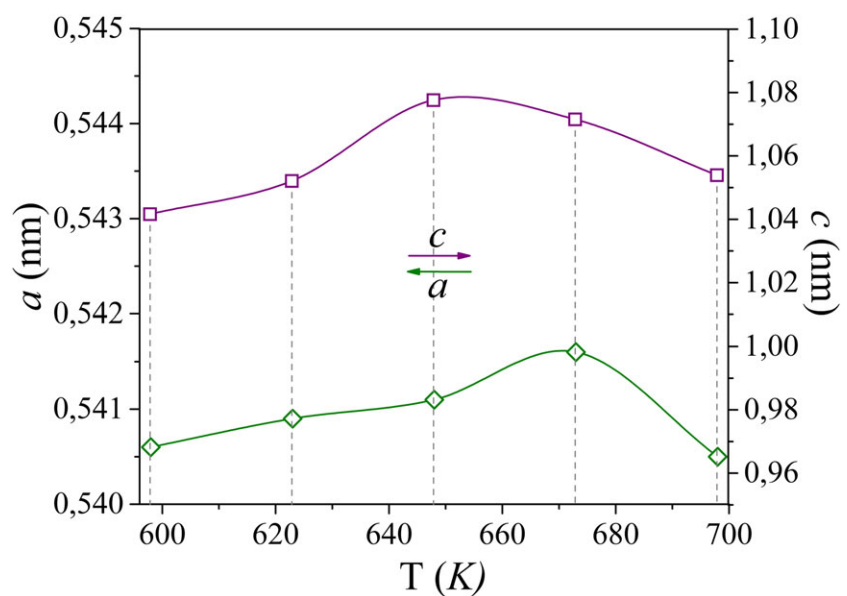
FIGURE 3 Dependence of lattice parameters (a, c) from the deposition temperature
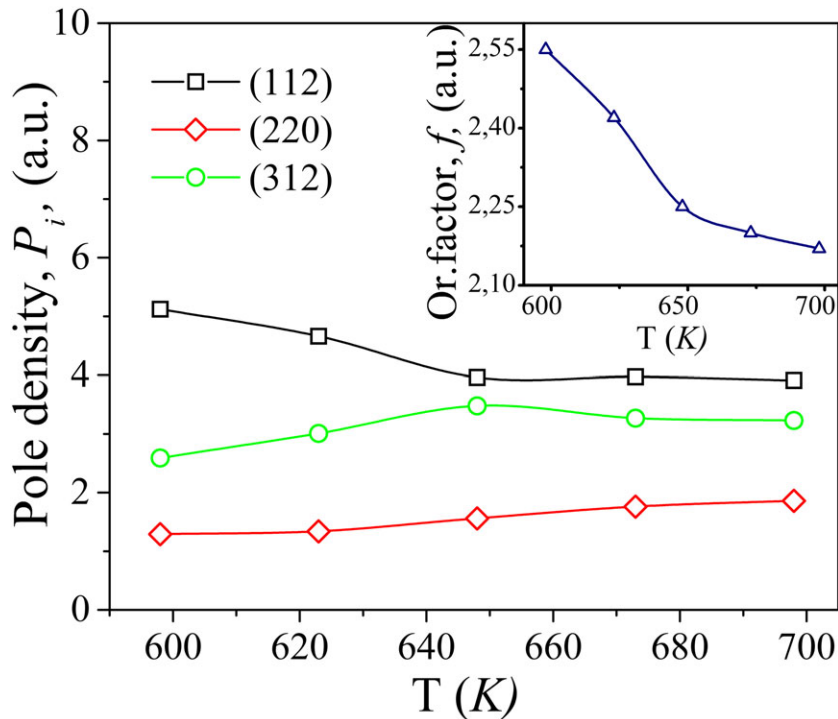
FIGURE 4 Dependence of P_i and f (inset) from deposition temperatures
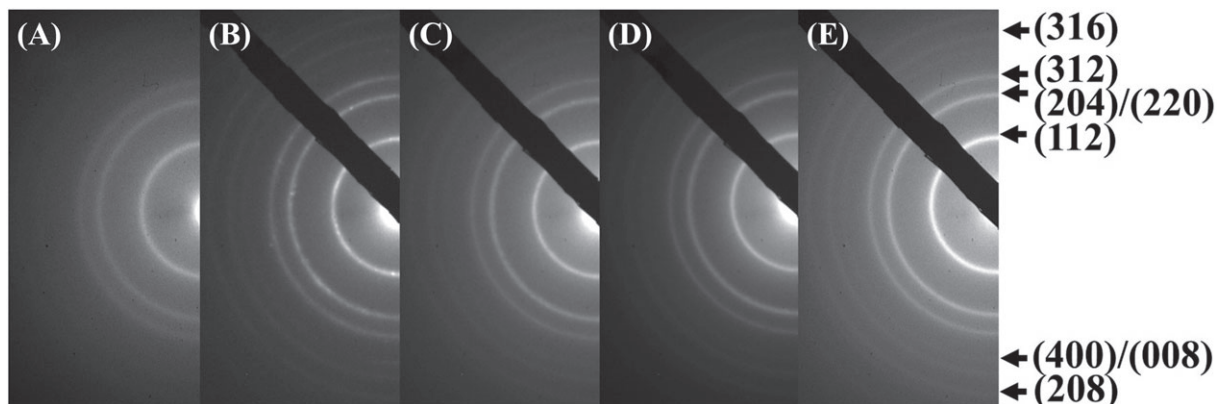
**FIGURE 5** Selected area diffraction (SAED) patterns from thin films, deposited at T_S, K: 598 (A), 623 (B), 648 (C), 673 (D), 698 (E)

(SAED) patterns are presented in Figure 5. In the SAED patterns, the polycrystalline diffraction rings were found, which correspond to the reflection from the tetragonal crystallographic planes with the kesterite-type phase for CZTS (card no. 00-026-0575) and CZGeS (card no. 01-078-0781), namely, (112), (204)/(220), (312), (400)/(008), and (208). The obtained results are well correlated with previous data from XRD measurements and the literature data.[38]

The typical Raman spectra for each of the deposition temperatures within a spectral range of the main peaks after the mapping process are shown in Figure 6A. According to the equation for $1/a$ (a is absorption coefficient of the material), the penetration depth of the laser radiation at the wavelength of $\lambda = 785$ nm is ≈ 287 nm for CZTS and ≈ 769 nm for CZGeS. Therefore, the penetration depth of a scanning near-infrared laser in our CZTGeS thin films was in the range from 287 to 769 nm, which is close to the total thicknesses of the films (700-800 nm). As can be seen from Figure 6A, the spectra obtained from each of the samples point to a single-phase kesterite-type structure without secondary phases. In the obtained spectra, peaks were detected, corresponding to the main phonon modes of CZTGeS, such as A_1, A_2, and B, which were in the range of 334 to 339, 301 to 305, and 368 to 376 cm^{-1}, respectively. The most intense peaks corresponding to the phonon modes A_1 and B occupy positions that are close to the previously reported experimental results for CZTGeS compound with a similar value of Ge/VI.[39,40] The position of A_1 symmetry mode in the range of 301 to 305 cm^{-1} is predominantly related to the rotational motion along the c-axis of Ge–S tetrahedra.[41]

Previously, in Garcia-Llamas et al,[42] the authors proposed simple linear equations for an evaluation of correlations between the Ge/(Ge + Sn) ratio and the Raman shift. Namely, according to the following equations,
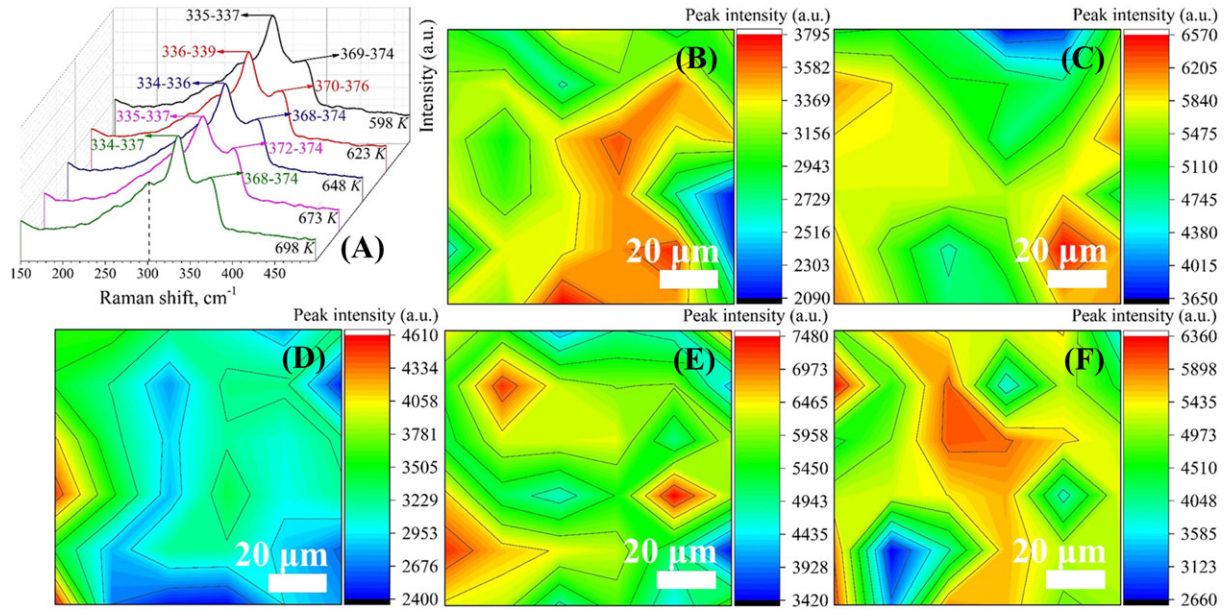
FIGURE 6 The typical Raman spectra for each deposition temperature (A) and Raman spectroscopy (RS) mapping analysis: (B—598 K, C—623 K, D—648 K, E—673 K, F—698 K)

$$\omega\left[cm^{-1}\right] = 287.0 + 9.1 \left(\frac{Ge}{Ge + Sn}\right), \tag{8}$$

and,

$$\omega\left[cm^{-1}\right] = 338.0 + 19.4 \left(\frac{Ge}{Ge + Sn}\right), \tag{9}$$

at Ge/(Ge + Sn) ≈ 0.3, vibrations of A_1 and A_2 symmetry modes should be positioned of 289 and 343 cm^{-1}, respectively. However, in our case, a shift in the position of each phonon mode towards a smaller value was observed in the spectra of different films, which is due to changes in the stoichiometric composition and strains. The EDS and XRD methods have confirmed these results.

Figure 6B-F shows the RS-mapping analysis of CZTGeS thin films, deposited at different temperatures. Since the ratio values of the most intense modes A_2 and B in spectra were almost unchanged at different measuring points, a phonon mode A_2 was selected for a clear demonstration of changes in the films, depending on temperature. In order to reach this aim, 36 different points with a step of 20 μm were scanned in coordinates X and Y over the film's surface. As can be seen from the maps (Figure 6B-F), the changing of deposition temperature affects the peak intensity. For a thin film deposited at T_S = 598 K (Figure 6 B), the maximum intensity of the phonon mode A_2 does not exceed 4000 a.u., but for the next temperature regime of T_S = 623 K (Figure 6C), this intensity corresponds to the minimum value on the scale. Increasing of T_S up to 648 K (Figure 6D) contributes to the more uniform distribution of intensities on the scanned area. However, the values of intensity are lower than in the previous temperature regime. In Figure 6E,F, corresponding to the temperature regimes of T_S = 673 K and T_S = 698 K, respectively, the intensity distributions are clearly seen, in accordance with the surface morphology. The lowest

intensities in the figures correspond to the deep craters that were previously studied by the AFM method. At the same time, the intensity of the phonon mode A_2 on smooth sections of these films have the highest values on the scale.

Raman spectra obtained with a near-infrared laser showed that thin films, deposited at different temperatures, have a single-phase kesterite-type structure. The changing of deposition temperature affects the vibration intensity of the main phonon mode A_2. The intensity is also changing depending on the surface morphology of the films.

Thus, CZTGeS film, deposited at T_S = 623 K, showed better characteristics. It has demonstrated a single-phase tetragonal crystal structure with a relatively large grain size, good texture quality and equilibrium orientation of crystallites.

3.3 | Optical properties

In order to determine the absorption coefficient (α), the transmittance spectra of CZTGeS films were studied in the range of wavelength of λ = 340 to 1000 nm. The results are presented in Figure 7A. Analysis of the transmittance spectra shows that CZTGeS films have a relatively weak transmittance, which does not exceed 50%. It is a desirable property for using of such a thin film in solar cells as an absorber layer. At the same time, increasing of deposition temperature reduced the transmittance of the films by 10%, except the sample obtained at 698 K. The dependence of $(\alpha h\upsilon)^2$ on $h\upsilon$ was constructed for a reliable determination of the optical band gap. The corresponding curves are shown in Figure 7B.

It was found that the optical band gap decreases from 1.89 to 1.84 eV with increasing of the deposition temperature. In our case, the shrinkage of lattice did not enlarge the band gap for films
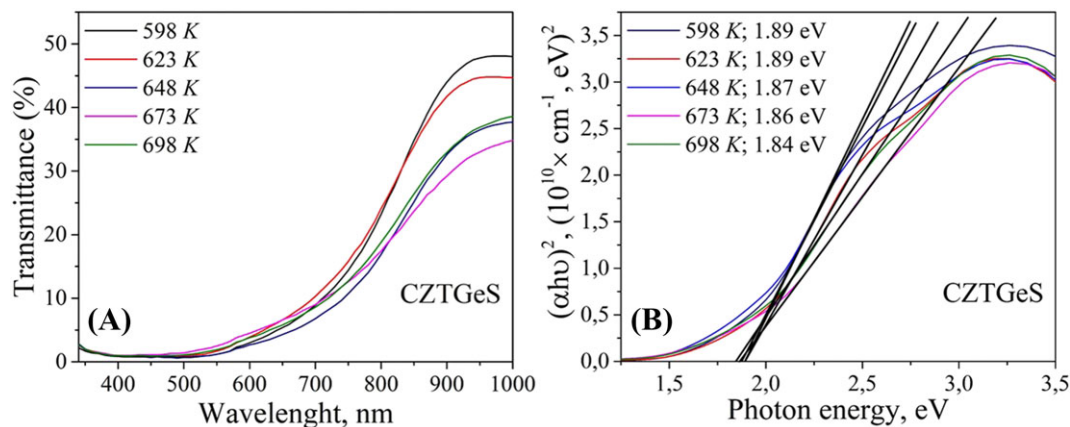
FIGURE 7 Transmittance spectra (A) and plot of $(\alpha h\upsilon)^2 = f(h\upsilon)$ (B) for determination of the optical band gap of CZTGeS thin films

deposited at T_S = 673 K and T_S = 698 K, contrary to the findings described by other authors.[43] It is due to a small variation in the values of the lattice parameters (only in the third place after the decimal point), which is confirmed by the XRD method. The estimated range of 1.84 to 1.89 eV is well correlated with the literature data for CZTGeS compound.[16]

4 | CONCLUSIONS

In summary, the chemically prepared thin films were investigated by AFM, EDS, TEM, XRD, RS-mapping, and optical methods. It was found that changes in the deposition temperature affect the surface morphology of thin films. At deposition temperatures of T_S = 673 K and T_S = 698 K, the formation of deep craters are observed, which leads to an increasing of RMS and ASR parameters to maximum values. In the temperature region of T_S = 623 to 648 K, crystallization of the material with an average crystallites diameter of 16 to 17 nm is observed. As-deposited thin films were Cu and Zn rich, but S poor. The maximum value of the Ge/Sn + Ge ratio was observed in the film deposited at T_S = 623 K. It was found that each sample has a tetragonal crystal structure with a kesterite-type phase of CZTGeS. The volume of the crystal lattice is increased with increasing of temperature up to 648 K, which is explained by the increasing of the concentration of Sn atoms in the sample. However, the lattice shrinkage effect has been identified at higher deposition temperatures (T_S = 673 K and T_S = 698 K), which is due to the rapid replacing of Sn atoms by Ge atoms in the crystal lattice. It was found that an axial texture growth occurs preferably in the (112) direction. Increasing of the deposition temperature leads to increasing of texture growth in the directions of crystallographic planes (220) and (312). The sample deposited at T_S = 623 K has the equilibrium orientation of crystallites in the crystallographic planes of (112), (220), and (312). A shift in the position of each phonon mode towards a smaller value was observed in RS spectra of films, deposited in different temperature regimes, which is due to the changes in stoichiometric composition and strains. The RS-mapping analysis indicates that the deposition temperature affects the intensity of vibrations of A_2 symmetry mode. Raman maps show

the distribution of intensities of CZTGeS modes in accordance with the surface morphology. The transmittance spectra have revealed the fact that increasing of the deposition temperature leads to a monotonous decreasing of the optical band gaps from 1.89 to 1.84 eV.

ORCID

A. Shamardin https://orcid.org/0000-0002-1646-7356
D. Kurbatov https://orcid.org/0000-0002-2754-6367

REFERENCES

1. Green MA, Hishikawa Y, Dunlop ED, Levi DH, Hohl-Ebinger J, Ho-Baillie AWY. Solar cell efficiency tables (version 52). *Prog Photovoltaics Res Appl.* 2018;26(7):427-436. https://doi.org/10.1002/pip.3040

2. Liu X, Feng Y, Cui H, et al. The current status and future prospects of kesterite solar cells: a brief review. *Prog Photovoltaics Res Appl.* 2016;24(6):879-898. https://doi.org/10.1002/pip.2741

3. Yan C, Huang J, Sun K, et al. Cu$_2$ZnSnS$_4$ solar cells with over 10% power conversion efficiency enabled by heterojunction heat treatment. *Nat Energy*. 2018. https://doi.org/10.1038/s41560-018-0206-0;3(9):764-772.

4. Liu F, Huang J, Sun K, et al. Beyond 8% ultrathin kesterite Cu$_2$ZnSnS$_4$ solar cells by interface reaction route controlling and self-organized nanopattern at the back contact. *NPG Asia Mater*. 2017;9(7). https://doi.org/10.1038/am.2017.103

5. Márquez J, Stange H, Hages CJ, et al. Chemistry and dynamics of Ge in Kesterite: toward band-gap-graded absorbers. *Chem Mater.* 2017;29(21):9399-9406. https://doi.org/10.1021/acs.chemmater.7b03416

6. Hurtado M, Cruz SD, Becerra RA, Calderón C, Gordillo G. XPS analysis and structural characterization of CZTS thin films prepared using solution and vacuum based deposition techniques. *Ieee Pvsc*. 2014;40:2-6. https://doi.org/10.1109/PVSC.2014.6924934

7. Zhang Y, Tse K, Xiao X, Zhu J. Controlling defects and secondary phases of CZTS by surfactant potassium. *Phys Rev Mater*. 2017;1(4). https://doi.org/10.1103/PhysRevMaterials.1.045403

8. Just J, Sutter-Fella CM, Lützenkirchen-Hecht D, Frahm R, Schorr S, Unold T. Secondary phases and their influence on the composition of the kesterite phase in CZTS and CZTSe thin films. *Phys Chem Chem Phys*. 2016;18(23):15988-15994. https://doi.org/10.1039/c6cp00178e

9. Ford GM, Guo Q, Agrawal R, Hillhouse HW. Earth abundant element $Cu_2Zn(Sn_{1-x}Ge_x)S_4$ nanocrystals for tunable band gap solar cells: 6.8% efficient device fabrication. *Chem Mater*. 2011;23(10):2626-2629. https://doi.org/10.1021/cm2002836

10. Caballero R, Victorov I, Serna R, et al. Band-gap engineering of $Cu_2ZnSn_{1-x}Ge_xS_4$ single crystals and influence of the surface properties. *Acta Mater*. 2014;79:181-187. https://doi.org/10.1016/j.actamat.2014.06.040

11. Shu Q, Yang J-H, Chen S, et al. $Cu_2Zn(Sn,Ge)Se_4$ and $Cu_2Zn(Sn,Si)Se_4$ alloys as photovoltaic materials: structural and electronic properties. *Phys Rev B*. 2013;87(11):115208. https://doi.org/10.1103/PhysRevB.87.115208

12. Khadka DB, Kim J. Band gap engineering of alloyed $Cu_2ZnGe_xSn_{1-x}Q_4$ (Q = S,Se) films for solar cell. *J Phys Chem C*. 2015;119(4):1706-1713. https://doi.org/10.1021/jp510877g

13. Chen J, Li W, Yan C, Huang S, Hao X. Studies of compositional dependent $Cu_2Zn(Ge_xSn_{1-x})S_4$ thin films prepared by sulfurizing sputtered metallic precursors. *J Alloys Compd*. 2015;621:154-161. https://doi.org/10.1016/j.jallcom.2014.09.097

14. Fu H. Environmentally friendly and earth-abundant colloidal chalcogenide nanocrystals for photovoltaic applications. *J Mater Chem C*. 2018;6(3):414-445. https://doi.org/10.1039/c7tc04952h

15. Fella CM, Romanyuk YE, Tiwari AN. Technological status of $Cu_2ZnSn(S,Se)_4$ thin film solar cells. *Sol Energy Mater Sol Cells*. 2013;119:276-277. https://doi.org/10.1016/j.solmat.2013.08.027

16. Peng X, Zhang S, Xiang Y. Solvothermal synthesis of $Cu_2Zn(Sn_{1-x}Ge_x)S_4$ and $Cu_2(Sn_{1-x}Ge_x)S3$ nanoparticles with tunable band gap energies. *J Alloys Compd*. 2015;640:75-81. https://doi.org/10.1016/j.jallcom.2015.03.248

17. Khadka DB, Kim J. Study of structural and optical properties of kesterite Cu_2ZnGeX_4 (X = S, Se) thin films synthesized by chemical spray pyrolysis. *CrstEngComm*. 2013;15(48):10500. https://doi.org/10.1039/c3ce41387j

18. Nguyen TH, Fujikawa S, Harada T, Chantana J. Impact of precursor compositions on the structural and photovoltaic properties of spray-deposited Cu_2ZnSnS_4 thin films. *ChemSusChem*. 2016;18:2414-2420. https://doi.org/10.1002/cssc.201600641

19. Eslamian M. Spray-on thin film PV solar cells: advances, potentials and challenges. *Coatings*. 2014;4(1):60-84. https://doi.org/10.3390/coatings4010060

20. Berestok TO, Kurbatov DI, Opanasyuk NM, Pogrebnjak AD, Manzhos OP, Danilchenko SM. Structural properties of ZnO thin films obtained by chemical bath deposition technique. *Journal of Nano- and Electronic Physics*. 2013;5(1):4-7.

21. Harris GB. X. Quantitative measurement of preferred orientation in rolled uranium bars. *London, Edinburgh, Dublin Philos Mag J Sci*. 1952;43(336):113-123. https://doi.org/10.1080/14786440108520972

22. Pantoja Enriquez J, Mathews NR, Pérez Hernández G, Mathew X. Influence of the film thickness on structural and optical properties of CdTe thin films electrodeposited on stainless steel substrates. *Mater Chem Phys*. 2013;142(1):432-437. https://doi.org/10.1016/j.matchemphys.2013.07.043

23. Kim KH, Chun JS. X-ray studies of SnO_2 prepared by chemical vapour deposition. *Thin Solid Films*. 1986;141(2):287-295. https://doi.org/10.1016/0040-6090(86)90356-1

24. Kumarasinghe PKK, Dissanayake A, Pemasiri BMK, Dassanayake BS. Effect of post deposition heat treatment on microstructure parameters, optical constants and composition of thermally evaporated CdTe thin films. *Mater Sci Semicond Process*. 2017;58(August 2016):51-60. https://doi.org/10.1016/j.mssp.2016.11.028

25. Prabhakar T, Nagaraju J. Ultrasonic spray pyrolysis of CZTS solar cell absorber layers and characterization studies. *Conf Rec IEEE Photovolt Spec Conf*. 2010;xx:1964-1969. https://doi.org/10.1109/PVSC.2010.5616709

26. Fadavieslam MR, Keshavarz S. Effects of growth temperatures on the physical properties of Cu_2ZnSnS_4 thin films deposited through spray pyrolysis for solar cell applications. *Appl Phys a*. 2018;124(2):163. https://doi.org/10.1007/s00339-018-1591-8

27. Shamardin A V., Opanasyuk AS, Kurbatov DI, Medvids A. The effect of laser processing on the structural characteristics and elemental composition of CZTS thin film obtained by spray pyrolysis method. In: 2nd International Conference on Information and Telecommunication Technologies and Radio Electronics, UkrMiCo 2017 - Proceedings. ; 2017:1–4. doi:https://doi.org/10.1109/UkrMiCo.2017.8095397.

28. Goldstein JI, Newbury DE, Echlin P, et al. *Scanning Electron Microscopy and X-Ray Microanalysis*. 3rd ed. Boston, MA: Springer US; 2003. https://doi.org/10.1007/978-1-4615-0215-9

29. Caballero R, Cano-Torres JM, Garcia-Llamas E, et al. Towards the growth of $Cu_2ZnSn_{1-x}Ge_xS_4$ thin films by a single-stage process: effect of substrate temperature and composition. *Sol Energy Mater Sol Cells*. 2015;139:1-9. https://doi.org/10.1016/j.solmat.2015.03.004

30. Kattan N, Hou B, Fermín DJ, Cherns D. Crystal structure and defects visualization of Cu_2ZnSnS_4 nanoparticles employing transmission electron microscopy and electron diffraction. *Appl Mater Today*. 2015;1(1):52-59. https://doi.org/10.1016/j.apmt.2015.08.004

31. Zhou B, Xia D, Wang Y. Phase-selective synthesis and formation mechanism of CZTS nanocrystals. *RSC Adv*. 2015;5(86):70117-70126. https://doi.org/10.1039/C5RA11890E.

32. Camara SM, Wang L, Zhang X. Easy hydrothermal preparation of Cu_2ZnSnS_4 (CZTS) nanoparticles for solar cell application. *Nanotechnology*. 2013;24(49):495401. https://doi.org/10.1088/0957-4484/24/49/495401

33. Chen S, Walsh A, Gong XG, Wei SH. Classification of lattice defects in the kesterite Cu_2ZnSnS_4 and $Cu_2ZnSnSe_4$ earth-abundant solar cell absorbers. *Adv Mater*. 2013;25(11):1522-1539. https://doi.org/10.1002/adma.201203146

34. Waseda Y, Matsubara E, Shinoda K. *X-Ray Diffraction Crystallography*. Berlin, Heidelberg: Springer Berlin Heidelberg; 2011 https://doi.org/10.1007/978-3-642-16635-8.

35. Li J, Shen H, Chen J, Li Y, Yang J. Growth mechanism of Ge-doped CZTSSe thin film by sputtering method and solar cells. *Phys Chem Chem Phys*. 2016;18(41):28829-28834. https://doi.org/10.1039/C6CP05671G

36. Schorr S, Gonzalez-Aviles G. In-situ investigation of the structural phase transition in kesterite. *Phys Status Solidi*. 2009;206(5):1054-1058. https://doi.org/10.1002/pssa.200881214

37. Mariappan R, Ponnuswamy V, Chandra Bose A, Chithambararaj A, Suresh R, Ragavendar M. Structural, optical and electrical characterization of nebulizer-sprayed ZnO nano-rods. *Superlattices Microstruct*. 2014;65:184-194. https://doi.org/10.1016/j.spmi.2013.10.005

38. Kim I, Kim K, Oh Y, et al. Bandgap-graded $Cu_2Zn(Sn_{1-x}Ge_x)S_4$ thin-film solar cells derived from metal chalcogenide complex ligand capped nanocrystals. *Chem Mater*. 2014;26(13):3957-3965. https://doi.org/10.1021/cm501568d.

39. Cano-Torres JM, Caballero R, Victorov I, et al. Raman characterization and modelling of $Cu_2ZnSn_{1-x}Ge_xS_4$ single crystals grown using

chemical vapor transport. *Opt Mater (Amst)*. 2017;66:671-677. https://doi.org/10.1016/j.optmat.2017.03.016

40. Valakh MY, Litvinchuk AP, Dzhagan VM, et al. Optical properties of quaternary kesterite-type $Cu_2Zn(Sn_{1-x}Ge_x)S_4$ crystalline alloys: Raman scattering, photoluminescence and first-principle calculations. *RSC Adv*. 2016;6(72):67756-67763. https://doi.org/10.1039/C6RA13608G

41. Guc M, Litvinchuk AP, Levcenko S, et al. Optical phonons in the kesterite Cu_2ZnGeS_4 semiconductor: polarized Raman spectroscopy and first-principle calculations. *RSC Adv*. 2016;6(16):13278-13285. https://doi.org/10.1039/C5RA26844C

42. Garcia-Llamas E, Guc M, Bodnar IV, et al. Multiwavelength excitation Raman scattering of $Cu_2ZnSn_{1-x}Ge_x(S,Se)_4$ single crystals for earth abundant photovoltaic applications. *J Alloys Compd*. 2017;692:249-256. https://doi.org/10.1016/j.jallcom.2016.09.035

43. He J, Sun L, Ding N, et al. Single-step preparation and characterization of $Cu_2ZnSn(S_xSe_{1-x})_4$ thin films deposited by pulsed laser deposition method. *J Alloys Compd*. 2012;529:34-37. https://doi.org/10.1016/j.jallcom.2012.03.065